Dislocation Damping and Anisotropic Seismic Wave Attenuation in Earth's Upper Mantle

Robert J. M. Farla *et al.*

Science **336**, 332 (2012);
DOI: 10.1126/science.1218318

Science (print ISSN 0036-8075; online ISSN 1095-9203) is published weekly, except the last week in December, by the American Association for the Advancement of Science, 1200 New York Avenue NW, Washington, DC 20005.

source and drain electrodes. Figure 4B displays a comparison of the transfer characteristics of both TFTs. In the TFTs with PEIE-coated source and drain electrodes, V_{TH} dropped from 4.5 to 0.4 V, the average μ increased from 0.04 to 0.1 $cm^2 V^{-1} s^{-1}$ and the device yield improved from 60% to 95%. We note that whereas μ values obtained after the PEIE modification are comparable to those of similar TFTs previously reported, the V_{TH} in our devices is lower (*4*). In this example, PEIE also coats the gate insulator inside the channel. PEIE layers thicker than 1.5 nm led to n-doping of the organic semiconductor channel. Similar doping was also observed on bottom-gate bottom-contact $PC_{60}BM$ TFTs that used PEIE-coated Au electrodes with PEIE thicknesses greater than 10 nm (fig. S14). This doping could assist the injection/collection of carriers by producing band-bending in the vicinity of the conductor surface; this effect is also likely present in OSCs containing fullerene-based acceptors (Fig. 3).

In a second example, bottom-gate top-contact amorphous InGaZnO (IGZO) TFTs were fabricated as shown in Fig. 4C. In contrast to the devices described above, PEIE was first deposited directly on top of the semiconductor (to prevent any damage from the radio frequency–sputtering deposition of IGZO) and the Au source and drain electrodes were evaporated on top of the PEIE layer. Figure 4D provides a comparison of the transfer characteristics of IGZO TFTs with and without PEIE. As in the n-channel organic-based TFTs, the V_{TH} of the IGZO TFTs dropped from 38.7 to 1.5 V and μ increased from 0.004 to 1.2 $cm^2 V^{-1} s^{-1}$ in the devices with the PEIE-modified electrodes.

Finally, we tested the use of PEIE in OLEDs by replacing a LiF/Al cathode with PEIE/Al in benchmark devices based on 4,4′-bis(carbazol-9-yl)biphenyl (CBP) and an emitter of *fac*-tris(2-phenylpyridinato-$N,C^{2'}$) iridium [$Ir(ppy)_3$], and achieved an external quantum efficiency of 15% (fig. S15). Although the performance of these devices was not optimized, it illustrates the applicability of this method to OLED platforms.

Polymers containing simple aliphatic amine groups such as PEIE and PEI appear to be "universal" surface modifiers that allow the fabrication, at very low cost and from environmentally friendly solvents, of air-stable low-WF electrodes. This approach should enable the mass production of low-WF electrodes from processes that are compatible with the large-area roll-to-roll manufacturing techniques required for the commercialization of low-cost organic and printed electronic devices. The specific properties of the polymers can be further optimized for other applications, and conceptually the approach could be applied to the development of polymers for high-WF electrodes.

References and Notes

1. H. Y. Chen *et al.*, *Nat. Photonics* **3**, 649 (2009).
2. R. H. Friend *et al.*, *Nature* **397**, 121 (1999).
3. G. Yu, J. Gao, J. C. Hummelen, F. Wudl, A. J. Heeger, *Science* **270**, 1789 (1995).
4. H. Yan *et al.*, *Nature* **457**, 679 (2009).
5. H. Cheun *et al.*, *J. Phys. Chem. C* **114**, 20713 (2010).
6. L. Wang *et al.*, *Nat. Mater.* **5**, 893 (2006).
7. J. Meyer *et al.*, *Appl. Phys. Lett.* **93**, 073308 (2008).
8. H. Cheun *et al.*, *Opt. Express* **18** (suppl. 4), A506 (2010).
9. F. Nüesch, L. J. Rothberg, E. W. Forsythe, Q. T. Le, Y. Gao, *Appl. Phys. Lett.* **74**, 880 (1999).
10. W. Osikowicz *et al.*, *Appl. Phys. Lett.* **85**, 1616 (2004).
11. L. Lindell *et al.*, *Appl. Phys. Lett.* **92**, 163302 (2008).
12. B. Bröker *et al.*, *Appl. Phys. Lett.* **93**, 243303 (2008).
13. L. Lindell *et al.*, *Chem. Mater.* **18**, 4246 (2006).
14. F. L. E. Jakobsson *et al.*, *Chem. Phys. Lett.* **433**, 110 (2006).
15. A. Sharma, P. J. Hotchkiss, S. R. Marder, B. Kippelen, *J. Appl. Phys.* **105**, 084507 (2009).
16. X. Bulliard *et al.*, *Adv. Funct. Mater.* **20**, 4381 (2010).
17. S.-N. Hsieh *et al.*, *Org. Electron.* **10**, 1626 (2009).
18. J. Huang, Z. Xu, Y. Yang, *Adv. Funct. Mater.* **17**, 1966 (2007).
19. Y. Zhou *et al.*, *Sol. Energy Mater. Sol. Cells* **93**, 497 (2009).
20. G. Jo *et al.*, *Appl. Phys. Lett.* **97**, 213301 (2010).
21. S. I. Na *et al.*, *Appl. Phys. Lett.* **97**, 223305 (2010).
22. See supplementary materials on *Science* Online.
23. F. Huang, H. B. Wu, Y. Cao, *Chem. Soc. Rev.* **39**, 2500 (2010).
24. F. Huang *et al.*, *Adv. Mater.* **19**, 2010 (2007).
25. S. H. Oh, D. Vak, S.-I. Na, T.-W. Lee, D.-Y. Kim, *Adv. Mater.* **20**, 1624 (2008).
26. W. Ma *et al.*, *Adv. Mater.* **17**, 274 (2005).
27. R. Schlapak *et al.*, *Langmuir* **23**, 8916 (2007).
28. G. Latini, M. Wykes, R. Schlapak, S. Howorka, F. Cacialli, *Appl. Phys. Lett.* **92**, 013511 (2008).
29. G. Heimel, L. Romaner, J.-L. Brédas, E. Zojer, *Phys. Rev. Lett.* **96**, 196806 (2006).
30. G. Heimel, L. Romaner, E. Zojer, J.-L. Brédas, *Acc. Chem. Res.* **41**, 721 (2008).
31. H. Li, P. Paramonov, J.-L. Brédas, *J. Mater. Chem.* **20**, 2630 (2010).
32. Y. He, H.-Y. Chen, J. Hou, Y. Li, *J. Am. Chem. Soc.* **132**, 1377 (2010).
33. H. Schmidt *et al.*, *Appl. Phys. Lett.* **96**, 243305 (2010).
34. A. Wagenpfahl, D. Rauh, M. Binder, C. Deibel, V. Dyakonov, *Phys. Rev. B* **82**, 115306 (2010).
35. Y. J. Cheng, C.-H. Hsieh, Y. He, C.-S. Hsu, Y. Li, *J. Am. Chem. Soc.* **132**, 17381 (2010).
36. Y. H. Zhou *et al.*, *Appl. Phys. Lett.* **97**, 153304 (2010).
37. O. Inganäs, *Nat. Photonics* **5**, 201 (2011).
38. S. Choi, W. J. Potscavage Jr., B. Kippelen, *Opt. Express* **18** (suppl. 3), A458 (2010).
39. A. Rolland, J. Richard, J. P. Kleider, D. Mencaraglia, *Jpn. J. Appl. Phys.* **35**, 4257 (1996).
40. D. K. Hwang *et al.*, *Adv. Mater.* **23**, 1293 (2011).

Acknowledgments: Supported by the Center for Interface Science: Solar Electric Materials, an Energy Frontier Research Center funded by the U.S. Department of Energy, Office of Science, Office of Basic Energy Sciences, under award DE-SC0001084 (Y.Z., J.S., J.M., H.C., H.L., P.W., S.B., J.-L.B., S.R.M., and S.G.), the NSF Science and Technology Centers program under agreement DMR-0120967 (C.F.-H., J.K., E.N., and A.D.), Office of Naval Research grant N00014-04-1-0120) (T.M.K. and B.K.), NSF grants DMR-1005892 (A.K.) and CMMI-0927736 (H.S.), the U.S. Department of Energy, Office of Science, Office of Basic Energy Sciences under award DE-FG02-05ER46165 (W.H. and T.P.), the Deutsche Forschungsgemeinschaft postdoctoral fellowship program (J.M.), and the National Defense Science and Engineering Graduate Fellowship program and NSF graduate research fellowship DGE-0644493 (A.J.G.).

Supplementary Materials

www.sciencemag.org/cgi/content/full/336/6079/327/DC1
Materials and Methods
Figs. S1 to S16
Tables S1 to S3
References (*41*–*52*)

6 January 2012; accepted 29 February 2012
10.1126/science.1218829

Dislocation Damping and Anisotropic Seismic Wave Attenuation in Earth's Upper Mantle

Robert J. M. Farla,[1]*† Ian Jackson,[1] John D. Fitz Gerald,[1] Ulrich H. Faul,[2] Mark E. Zimmerman[3]

Crystal defects form during tectonic deformation and are reactivated by the shear stress associated with passing seismic waves. Although these defects, known as dislocations, potentially contribute to the attenuation of seismic waves in Earth's upper mantle, evidence for dislocation damping from laboratory studies has been circumstantial. We experimentally determined the shear modulus and associated strain-energy dissipation in pre-deformed synthetic olivine aggregates under high pressures and temperatures. Enhanced high-temperature background dissipation occurred in specimens pre-deformed by dislocation creep in either compression or torsion, the enhancement being greater for prior deformation in torsion. These observations suggest the possibility of anisotropic attenuation in relatively coarse-grained rocks where olivine is or was deformed at relatively high stress by dislocation creep in Earth's upper mantle.

A rheologically weak sublithospheric mantle (the asthenosphere) is widely invoked to explain the motion of the tectonic plates on Earth [e.g., (*1*)]. Laboratory experiments underpin an emerging understanding of the anomalous seismic properties of the asthenosphere (*2*, *3*). In particular, the seismic anisotropy of this part of the upper mantle is attributed to crystallographic preferred orientation in olivine-rich rocks—testimony to their deformation by dislocation creep (*4*–*11*). Several studies have demonstrated that anelastic relaxation attributed to grain-boundary sliding can affect the shear modulus and attenuation of upper mantle rocks (*12*–*16*), but evidence for strain-energy dissipation from mechanically forced vibrations of dislocations has been largely circumstantial until now.

[1]Research School of Earth Sciences, Australian National University, Canberra, Australian Capital Territory 0200, Australia. [2]Department of Earth Sciences, Boston University, Boston, MA 002215, USA. [3]Department of Geology and Geophysics, University of Minnesota, Minneapolis, MN 55455, USA.

*To whom correspondence should be addressed. E-mail: robert.farla@yale.edu

†Present address: Department of Geology and Geophysics, Yale University, New Haven, CT 06520, USA.

Table 1. Specimen characterization. Uncertainty is calculated as 1 SD. wt. ppm, concentration of species by weight in parts per million.

Specimen	d_i* (μm)	d_f (μm)	ρ_i† (μm^{-2})	ρ_f (μm^{-2}) (Fig. 3)	Water content‡ (wt. ppm H_2O)	Forced oscillation conditions: Maximum flow stress (MPa)	Forced oscillation conditions: Maximum strain ($\times 10^{-5}$)
H6585	3.1 (1.8)	3.1 (1.4)	1.0 (0.7)	1.0 (0.9)	3/2	0.53	1.00
D6618	5.0 (2.6)	4.9 (2.5)	4.8 (1.6)	1.9 (0.8)	4/2	0.19	0.46
D6646	4.8 (2.6)	5.0 (3.2)	7.1 (1.8)	5.1 (2.0)	2/2	0.35	0.95
T0436	6.7 (4.7)	5.7 (3.7)	2.4 (1.0)	1.3 (1.1)	5/2	0.38	0.78

*Grain size d, where i and f indicate before and after forced-oscillation testing, respectively. †Dislocation density ρ, where i and f indicate before and after forced-oscillation testing, respectively. ‡Water content before/after forced-oscillation testing [calibration as in (*28*)].

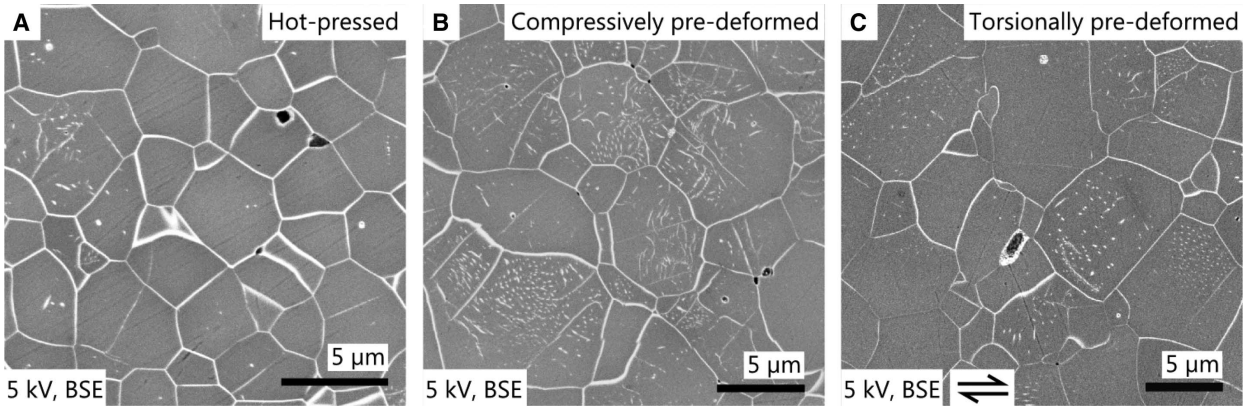

Fig. 1. Backscattered electron (BSE) micrographs of (**A**) a hot-pressed and un-deformed olivine specimen (H6585), (**B**) a compressively pre-deformed specimen (D6646), and (**C**) a torsionally pre-deformed specimen (T0436) after forced-oscillation testing. The dislocation density increased during deformation and remained higher than a that of a hot-pressed specimen after forced-oscillation testing. The average grain size is typically from 3 to 6 μm.

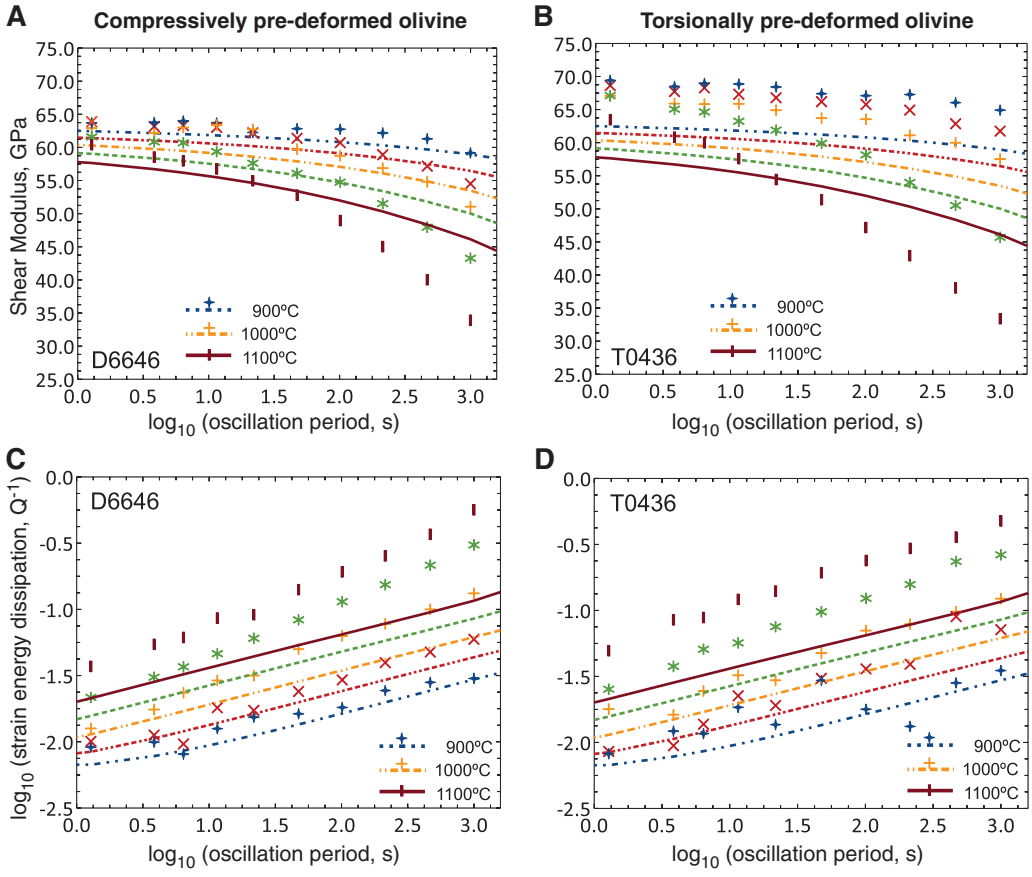

Fig. 2. Shear modulus (**A** and **B**) and dissipation (**C** and **D**) plotted against $\log_{10}$(oscillation period) for selected pre-deformed sol-gel olivine specimens, color-coded for representative temperatures as follows: 1100°C (maroon), 1050°C (green), 1000°C (orange), 950°C (red), and 900°C (blue). The dashed curves represent a model involving a Burgers-type creep function fitted to data for a suite of un-deformed hot-pressed olivine specimens (*16*). The model was evaluated at the grain size relevant for each specimen. Shear moduli for specimen T0436 higher than the (isotropic) anharmonic value (66.5 GPa at 900°C) are tentatively attributed to elastic anisotropy associated with crystallographic preferred orientation.

A single exploratory study of dislocation damping to date has demonstrated enhanced strain-energy dissipation in favorably oriented pre-deformed specimens of single-crystal forsterite (*17*).

Following this promising lead, we present a systematic study of pre-deformed polycrystalline olivine to determine the influence of dislocation density on shear wave speeds and attenuation within Earth's upper mantle. We deformed olivine specimens in either triaxial compression or torsion to introduce populations of differently oriented dislocations. A simple analysis of the resolved shear stress for dislocation glide in polycrystalline olivine samples containing randomly oriented crystallites, pre-deformed in either compression or torsion, suggests that prior deformation in torsion is likely to yield higher levels of strain-energy dissipation in subsequent torsional oscillation tests (supplementary materials). The shear modulus (G) and strain-energy dissipation (Q^{-1}) were derived from the measured complex torsional compliance of experimental assemblies, each containing a deformed specimen, and were compared to a model fitted to equivalent data for a suite of undeformed (hot-pressed) olivine specimens, tested under similar conditions of temperature, pressure, and forced-oscillation period.

We performed microstrain forced torsional oscillation tests under conditions of simultaneous high temperature and pressure (*16*, *18*). Based on dislocation recovery rates measured in olivine at a range of temperatures under similar oxygen fugacity conditions (*19*), the conditions for forced-oscillation testing of the pre-deformed specimens were limited to 1100°C, at which recovery is expected to decrease the free dislocation density by only 10% over a period of 50 hours. We initially monitored the forced-oscillation response for several tens of hours at 200 MPa, confining pressure and the maximum temperature in order to ensure broadly stable grain-scale microstructure without excessive dislocation recovery. Thereafter, forced-oscillation tests at 1- to 1000-s periods were performed at selected temperatures, spaced by 25° to 200°C, during staged cooling to room temperature. A final excursion back to high-temperature conditions verified the reproducibility of the forced-oscillation data. The maximum shear stress at 1100°C during a 1000-s period of oscillation was about 0.5 MPa (Table 1), associated with a maximum strain of 1×10^{-5} (*20*), without any compelling evidence of nonlinear behavior associated, for example, with dislocation multiplication (*17*, *21*, *22*).

Microstructures of the hot-pressed and pre-deformed specimens, in particular the markedly different densities of dislocations, were imaged by backscattered electrons (Fig. 1). The reduction in dislocation density during high-temperature forced-oscillation testing was around 50% higher than predicted by a previous study of recovery kinetics (*19*). There was otherwise little microstructural evolution of the compressively pre-deformed specimens. A clean foam texture was preserved, with straight grain boundaries and only minor grain growth (Fig. 1 and Table 1). After the forced-oscillation testing, we found the torsionally pre-deformed specimen T0436 to have a somewhat smaller grain size and a more uniform fabric than before testing (fig. S4).

Forced-oscillation testing of both compressively and torsionally pre-deformed solution-gelation (sol-gel) olivine (supplementary materials) demonstrates a systematic reduction of shear modulus with increasing oscillation period and temperature (Fig. 2, A and B). We find a similar period dependence for Q^{-1} of both specimens (Fig. 2, C and D), with systematically and monotonically higher dissipation toward longer oscillation periods and higher temperatures. The G and Q^{-1} data from the more highly pre-deformed specimens (D6646 and T0436) are similar in many respects, consistent with their similar grain sizes. However, the final dislocation density of T0436 was lower by a factor of 4 and close to that of the hot-pressed specimen H6585 (Table 1). If we compare our data for the two more-highly pre-deformed specimens with a Burgers-type creep function (JF) model describing the behavior of undeformed but otherwise equivalent specimens (*16*), it becomes clear that the shear modulus measured on each of the pre-deformed specimens (Fig. 2, A and B) is more strongly period-dependent above 1000°C than in the JF model (Fig. 2). Also, G is higher at low temperature for the torsionally pre-deformed specimen, possibly reflecting elastic anisotropy associated with crystallographic preferred orientation (fig. S4). The dissipation measured for each pre-deformed specimen (Fig. 2, C and D) is substantially higher across the entire range of oscillation periods than in the JF model, especially at relatively high temperatures (Fig. 2). The increased dissipation and shear modulus dispersion of pre-deformed specimens as compared to the JF model for the behavior of undeformed specimens suggest that dislocations introduced during prior deformation are responsible for the substantial enhancement of a broad anelastic absorption band. We did not observe a dissipation peak that is diagnostic of a narrow distribution of relaxation times.

Overall, dissipation increased systematically with increasing strain or dislocation density in prior compressive deformation (D6618 and D6646) as compared to undeformed olivine (H6585) (Fig. 3). Furthermore, the torsionally pre-deformed specimen T0436 was 2.4 times as dissipative as a compressively pre-deformed specimen of the same final dislocation density (Fig. 3). The linear $Q^{-1}(\rho)$ trends

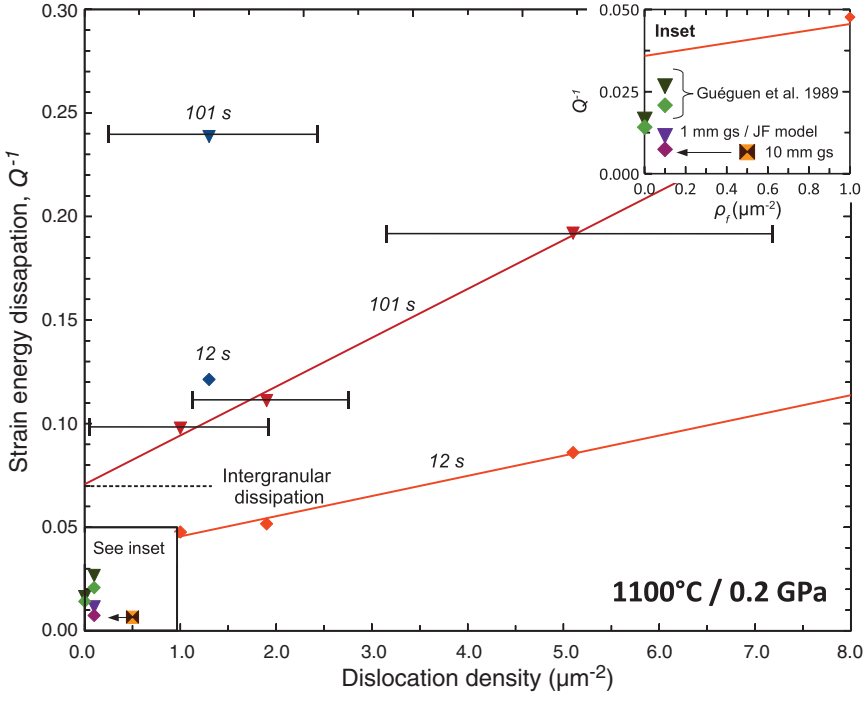

Fig. 3. Dissipation data (red/orange symbols) plotted against final dislocation density at 1100°C and 0.2 GPa confining pressure, for two representative oscillation periods: 12 s (inverted triangles) and 101 s (diamonds). Data for compressively pre-deformed olivine define the red linear trends, whose intercepts represent dissipation inferred for the intergranular relaxation processes acting alone. The data for torsionally pre-deformed olivine are shown by the blue symbols. The error bars attached to the 101-s data represent 1 SD for the population of estimates of dislocation density. Uncertainties in G and Q^{-1} are best estimated a posteriori from the scatter of the data around the generally systematic trends with varying oscillation period and temperature. Results from forced-oscillation testing on single-crystal forsterite (un-deformed and pre-deformed) are shown by the light- and dark-green symbols (*17*). The results of evaluating the JF model (*16*) for upper-mantle grain sizes (gs's) of 1 mm (purple inverted triangle for 101 s and magenta diamond for 12 s) and 10 mm (brown bowtie for 101 s and orange square for 12 s) are positioned at $\rho \sim 0.1\ \mu m^{-2}$ (see inset).

(where ρ is the dislocation density) for the hot-pressed and the compressively deformed specimens for the representative 12- and 101-s oscillation periods, which intercept the Q^{-1} axis at ~0.035 and 0.07 respectively, reflect contributions from intergranular relaxation processes, such as grain-boundary sliding, in the fine-grained (3 to 6 μm) polycrystalline olivines of this study. The additional dissipation, attributable to dislocation damping, was approximately $Q^{-1} = 0.024 \times \rho\ (\mu m^{-2})$ at a 101-s period for the compressively pre-deformed materials. Thus, dislocation damping may account for about 25% of the dissipation measured in the fine-grained (3.1 μm) hot-pressed specimen 6585.

In order to assess the relative contributions of these two dissipation mechanisms for the larger grain sizes expected of Earth's mantle, we used the previously mentioned JF model (*16*), describing the behavior of undeformed, essentially dry and melt-free polycrystalline olivine (including H6585), of average dislocation density ~0.1 μm^{-2}. This model, evaluated under laboratory conditions of 0.2 GPa and 1100°C and at the experimental periods near 12 and 101 s for representative upper-mantle grain sizes of 1 and 10 mm, yields values of Q^{-1} between 0.0065 and 0.0115 (Fig. 3, inset). Such dissipation is largely due to intergranular relaxation rather than dislocation damping. For compressively pre-deformed olivine tested at a 101-s period, comparable levels of dissipation would be expected from dislocation damping alone for upper-mantle dislocation densities of 0.3 to 0.5 μm^{-2}. The torsionally pre-deformed specimen (T0436) of the present study, with a population of dislocations similarly favorably oriented for glide, displayed much higher levels of dislocation damping than did compressively pre-deformed materials of comparable dislocation density. We conclude therefore that dislocation damping associated with typical upper-mantle dislocation densities (~0.01 to 0.1 μm^{-2}) (*10*, *23*) may contribute comparably with grain-boundary–related dissipation (with associated shear wave dispersion), especially in regions of Earth's upper mantle that are subject to relatively high prevailing (or fossil) deviatoric stress σ and consequently high dislocation density (*11*), and for shear waves with propagation/polarization directions that provide high resolved shear stress for dislocation glide.

Deformation in and beneath the oceanic lithosphere spreading away from a mid-ocean ridge involves simple shear in the vertical plane parallel to the spreading direction. This shear, if accomplished by glide on the dominant [100](010) slip system of olivine, will tend to result in rotation of the (010) planes of individual olivine crystals toward the horizontal so that [100] is preferentially aligned with the spreading direction. A crystallographic preferred orientation of this type, commonly measured in mantle xenoliths, provides the accepted explanation of the azimuthal anisotropy of compressional (P_n) wave speed (*6*, *24*, *25*). This fabric provides favorable average $V_{SH} > V_{SV}$ (V_{SH}, shear wave velocity with horizontal polarization; V_{SV}, shear wave velocity with vertical polarization) in transversely isotropic seismological wave speed models (*26*) that account for the discrepancy between Rayleigh and Love surface wave velocities (*27*). This fabric offers optimal average resolved shear stress for [100](010) dislocation glide for the geometry of the simple shear stress field controlling ongoing tectonic deformation beneath the oceanic plate. The same stress field applies to vertically travelling shear waves polarized parallel to the direction of plate motion direction. Accordingly, we predict that these seismic waves should be most strongly attenuated by dislocation glide in the suboceanic mantle.

Our data demonstrate that strain-energy dissipation (and shear modulus dispersion) associated with grain-boundary relaxation phenomena are augmented by the effects of dislocation relaxation. The relaxation strength is expected to vary linearly with the dislocation density, and in turn with the magnitude of the fossil/prevailing stress field as $\rho \propto \sigma^2$ (*11*). However, only in relatively cool parts of the lithosphere is a high dislocation density, reflecting a high fossil stress, likely to survive the process of static dislocation recovery. Under these circumstances, the relevant tectonic settings of high potential for dislocation damping will be regions in the lower lithosphere and asthenosphere, where olivine is or was deformed via (steady-state) dislocation creep. These regions include suboceanic mantle, deep-lithosphere shear zones, and the material immediately above and beneath an actively subducting slab.

References and Notes

1. D. L. Kohlstedt, B. Evans, S. J. Mackwell, *J. Geophys. Res.* **100**, 17587 (1995).
2. F. Cammarano, B. Romanowicz, *Geophys. J. Int.* **175**, 116 (2008).
3. C. A. Dalton, G. Ekström, A. M. Dziewonski, *Earth Planet. Sci. Lett.* **284**, 65 (2009).
4. I. M. Artemieva, M. Billien, J. Lévêque, W. D. Mooney, *Geophys. J. Int.* **157**, 607 (2004).
5. H. W. Green II, S. V. Radcliffe, *Earth Planet. Sci. Lett.* **15**, 239 (1972).
6. H. H. Hess, *Nature* **203**, 629 (1964).
7. S. Zhang, S. Karato, *Nature* **375**, 774 (1995).
8. A. Tommasi, D. Mainprice, G. Canova, Y. Chastel, *J. Geophys. Res.* **105**, 7893 (2000).
9. T. Mizukami, S. R. Wallis, J. Yamamoto, *Nature* **427**, 432 (2004).
10. C. Goetze, D. L. Kohlstedt, *J. Geophys. Res.* **78**, 5961 (1973).
11. J. B. Minster, D. L. Anderson, *Philos. Trans. R. Soc. Lond.* **299**, 319 (1981).
12. T. T. Gribb, R. F. Cooper, *J. Geophys. Res.* **103**, 27267 (1998).
13. R. F. Cooper, *Rev. Mineral. Geochem.* **51**, 253 (2002).
14. B. H. Tan, I. Jackson, J. D. Fitz Gerald, *Phys. Chem. Miner.* **28**, 641 (2001).
15. I. Jackson, U. H. Faul, J. D. Fitz Gerald, S. J. S. Morris, *Mater. Sci. Eng. A* **442**, 170 (2006).
16. I. Jackson, U. H. Faul, *Phys. Earth Planet. Inter.* **183**, 151 (2010).
17. Y. Gueguen, M. Darot, P. Mazot, J. Woirgard, *Phys. Earth Planet. Inter.* **55**, 254 (1989).
18. I. Jackson, M. S. Paterson, *Pure Appl. Geophys.* **141**, 445 (1993).
19. R. J. M. Farla *et al.*, *Phys. Chem. Miner.* **38**, 363 (2011).
20. I. Jackson, *Geophys. Res. Lett.* **20**, 2115 (1993).
21. Y. Gueguen, J. M. Mercier, *Phys. Earth Planet. Inter.* **7**, 39 (1973).
22. I. Jackson, in *Treatise on Geophysics,* G. Schubert, Ed. (Elsevier, Amsterdam, Netherlands, 2007), pp. 493–525.
23. M. Toriumi, *Contrib. Mineral. Petrol.* **68**, 181 (1979).
24. R. W. Raitt, G. G. Shor Jr., T. J. G. Francis, G. B. Morris, *J. Geophys. Res.* **74**, 3095 (1969).
25. D. Barnford, S. Crampin, *Geophys. J. R. Astron. Soc.* **49**, 1 (1977).
26. D. Mainprice, in *Treatise on Geophysics,* G. Schubert, Ed. (Elsevier, Oxford, 2007), vol. 2, pp. 437–492.
27. D. W. Forsyth, *Geophys. J. R. Astron. Soc.* **43**, 103 (1975).
28. M. S. Paterson, *Bull. Mineralogie* **105**, 20 (1982).

Acknowledgments: We thank H. Kokkonen, C. Saint, H. Miller, and F. Brink for experimental help and D. Kohlstedt for allowing us to use his laboratory at the University of Minnesota. The Australian government (an Endeavor International Postgraduate Research Scholarship), a Mervyn and Katalin Paterson Fellowship (Research School of Earth Sciences–Australian National University), and NASA grant NNX11AF58G supported this work. We thank three anonymous reviewers for helping to improve the manuscript. The raw data are available in the supplementary materials.

Supplementary Materials

www.sciencemag.org/cgi/content/full/336/6079/332/DC1
Materials and Methods
Figs. S1 to S4
Databases S1 to S5
References (*29*–*37*)

22 December 2011; accepted 20 March 2012
10.1126/science.1218318

Dynamic Causes of the Relation Between Area and Age of the Ocean Floor

N. Coltice,[1,2]* T. Rolf,[3] P. J. Tackley,[3] S. Labrosse[1,2]

The distribution of seafloor ages determines fundamental characteristics of Earth such as sea level, ocean chemistry, tectonic forces, and heat loss from the mantle. The present-day distribution suggests that subduction affects lithosphere of all ages, but this is at odds with the theory of thermal convection that predicts that subduction should happen once a critical age has been reached. We used spherical models of mantle convection to show that plate-like behavior and continents cause the seafloor area-age distribution to be representative of present-day Earth. The distribution varies in time with the creation and destruction of new plate boundaries. Our simulations suggest that the ocean floor production rate previously reached peaks that were twice the present-day value.

The distribution of ages of the ocean floor is a first-order observation that determines the evolution of Earth's surface and interior (*1*). Because heat flow and bathymetry directly depend on the age of the ocean floor (*2*), a shift in the area-age distribution profoundly modifies Earth's cooling (*3*), sea level (*4*, *5*), and consequently global climate (*6*, *7*). The characterization